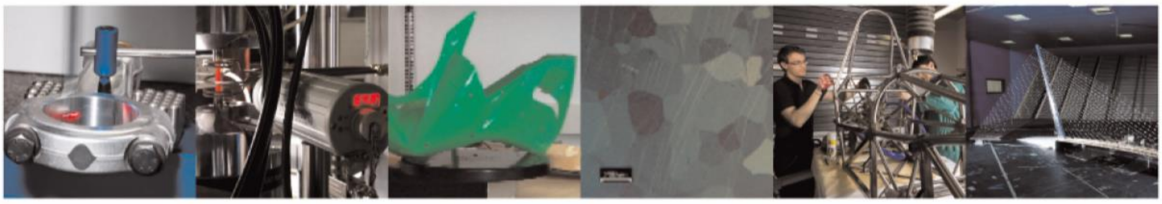

Selective laser melting Fe and Fe-35Mn for biodegradable implants

Carluccio, Danilo; Bermingham, Michael; Dargusch, M. S.; Demir, Ali Gökhan; Caprio, Leonardo; Previtali, Barbara

Electronic version of an article published as International Journal of Modern Physics B Vol. 34, No. 01n03, 2040034 (2020) https://doi.org/10.1142/S0217979220400342 © copyright World Scientific Publishing Company
https://www.worldscientific.com/doi/abs/10.1142/S0217979220400342

SELECTIVE LASER MELTING FE AND FE-35MN FOR BIODEGRADABLE IMPLANTS

Danilo Carluccio*, Michael Bermingham, M.S. Dargusch

School of Mechanical and Mining Engineering and Queensland Centre for Advanced Materials Processing and manufacturing (AMPMAP), The University of Queensland, St Lucia, QLD, 4072, Australia
**danilo.carluccio@uqconnect.edu.au*

Ali Gökhan Demir, Leonardo Caprio, Barbara Previtali

Department of Mechanical Engineering, Via la Masa 1,
Milan, 20156, Italy

Fe and Fe-based alloys are great candidates for biodegradable metal implants. In order to achieve high density pure Fe and Fe-35Mn structures, the correct implementation of process strategies and parameters needs to be studied to achieve high density parts. In this study pure Fe and Fe-35Mn were successfully processed via SLM with a relative density over 99.5 %. The lower melting temperature of Fe-35Mn introduced porosity, resulting in a lower processability compared to the pure Fe. In terms of process optimisation, most of the typical quality indicators (roughness, density, and apparent density) could be correlated to the energy density.

Keywords: Selective Laser Melting; Biodegradable Iron; Microstructure; Processing

1. Introduction

Fe and Fe-based alloys have shown potential recently as replacement materials for permanent metals used for temporary medical devices.[1] Temporary medical devices provide support during healing and subsequent to full healing. These devices are removed or left in the body, both of which can cause adverse reactions. Biodegradable metals can overcome these problems by providing the same support as permanent metals and when full healing is complete, degrade away leaving behind no residue in the implantation site. The bulk alloy constituents and degradation by-products must be fully biocompatible and non-toxic in the amounts released during degradation.[2] So far, the most researched biodegradable metals have been Mg, Zn and Fe and their alloys.[1,2]

The degradation rate of Mg is high compared to the other biodegradable metals and can be difficult to reliably predict.[3] Furthermore, there are safety concerns around the selective laser melting (SLM) of Mg. On the other hand, while the corrosion rate of Zn is deemed to be ideal for most biodegradable implants,[4] it often may not have suitable mechanical properties for load-bearing applications.[5] Unlike Zn, Fe has excellent mechanical properties, akin to the “gold standard” implant material 316L stainless steel. However, its degradation rate is often too slow and can behave like a permanent metal in the body.[6] The corrosion rate can be increased by additions of Mn to the alloy.[7] On top of this, the mechanical properties, formability and MRI compatibility are also improved by alloying with Mn.[8,9]

Fe implants are often manufactured using traditional manufacturing methods, requiring further post processing to obtain the final implant.[6] Selective laser melting can overcome this as it can produce highly customisable implants with complex geometries not achievable otherwise. Research on SLM of pure Fe has been relatively limited, since it has been mainly focused on the study of tool, maraging and other steels commonly used in industry.[10] Pure Fe was found to be relatively easy to process via SLM and have mechanical properties similar to cast Fe.[11,12] Pure Fe scaffolds have also been successfully manufactured using SLM and found to have improved corrosion rate and sufficient mechanical properties for bone scaffolds applications.[13]

An apparent lack of knowledge of the processability of biodegradable metals calls for further studies. By correctly implementing processing parameters, SLM can be used to manufacture implants not possible by means of conventional manufacturing. It is important to garner a greater understanding of the material processability, especially the effect of process parameters on the roughness, porosity and microstructure of the implant. Therefore, the aim of this paper is to investigate the ideal SLM processing conditions for biodegradable pure Fe and Fe-35Mn alloy for biodegradable implant applications.

2. Materials and Methods

2.1. *Materials and Selective Laser Melting System*

Samples were manufactured using the same gas atomised powder and under the same conditions as used in previous studies briefly described below. [14] The pure Fe powder had a 99.8 % purity and a particle size distribution of ≤45 µm (TLS Technik, Bitterfeld, Germany). Fe-35Mn samples were manufactured using gas atomised spherical Fe-35Mn alloy with a particle size distribution of ≤ 44 µm (CEAIT, San Sebastian, Spain).

SLM was performed using a Renishaw AM250 (Renishaw, Stone, UK). A 200 W single mode fibre laser was used throughout processing with an estimated beam size of 75 µm. In preparation for the build, a -950 mbar pressure was obtained by evacuating the chambers, followed by flooding of the chamber with Ar resulting in 15mbar of overpressure. Throughout the build the oxygen content was maintained below 1000 ppm.

2.2. *Design of Experiment*

A 2^3 factorial experimental plan with 3 central points was used to assess the optimum processing parameters for both alloys. To improve productivity the use of a maximum laser power (P) of 200 W was used. The focal position (f) and the layer thickness (z) were maintained constant throughout experiments at 0 mm and 50 µm respectively. The pulse duration (t_{on}) and point distance (d_p) of successive pulse wave (PW) emissions were varied along with the distance the beam jumps at the end of each vector to the next vector, named the hatch distance (d_h). The processing parameters used are shown in Table 1.

Table 1. Process parameters varied.

Varied parameters	Low	Mid	High
Pulse duration, t_{on} (µs)	80	100	120
Point distance d_p (µm)	40	60	80
Line distance, d_h (µm)	90	100	110

The energy density was calculated using:

$$E = \frac{P \cdot t_{on}}{d_p \cdot d_h \cdot z} \tag{1}$$

2.3. *Characterization*

SEM (EVO-50, Carl Zeiss, Germany) was used to characterise the surface of the as built samples. Surface roughness was measured using focus variation microscopy (InfiniteFocus, Alicona Imaging

GmbH, Austria). A real average surface roughness (S_a) was measured on the top surface of the as-built samples. A 5× objective lens was used to capture the whole surface with an axial and lateral resolution of 7 and 3.9 μm respectively. A short-pass Gaussian with cut-off length at 800 μm was used to obtain the roughness profile.

A procedure based on ISO 3369 was used to measure the density using Archimedes' method in air and H-Galden (ZT180, Solvay, Japan). The apparent density was measured using image processing software on images acquired of the cross section using optical microscopy (Polyvar Met, Reichert, USA). Samples were prepared by cutting cross sections perpendicular to the build direction, before mounting, grinding and polishing following standard metallographic procedures. The relative density was calculated using :

$$\rho_R(\%) = \left(1 - \frac{A_{Pore,tot}}{A_{tot}}\right) \cdot 100. \tag{2}$$

Where $A_{Pore,tot}$ is the total pore area and A_{tot} is the total area.

To observe the microstructure, samples were cut perpendicular and parallel to the build direction, mounted, ground, polished and etched with Nital. Optical microscopy and SEM (TM3030, Hitachi, Japan) were used to examine the microstructure. A linear intercept method based on ASTM E112-13 [15] was used to analyse the grain size of the pure Fe.

3. Results and Discussion

3.1. *Surface Morphology*

A general trend of decreasing S_a with increasing energy density can be observed for the Fe-35Mn as seen in Figure 1-A. Pure Fe follows a similar trend except at an energy density between 60-80 J/mm^3 where S_a reaches a sudden minimum that is lower than previous and subsequent points. At the lowest energy density, pure Fe and Fe-35Mn have the roughest surface morphologies composed of pores, partially sintered powder and balls (see Figure 2). The balling phenomena is characterised by small spherical balls that can be observed on selective laser melted surfaces. At lower energy densities the melt pool is smaller, therefore from the centre to edge of the melt pool there is a higher thermal gradient and higher surface tension gradient. This results in capillary instability which forms the small spherical balls seen on the surface.

The mechanism for balling at higher energy densities is different and caused by instability in the melt pool due to overheating resulting in small liquid droplets escaping from the melt pool.[16] At higher energy densities, less balling is observed on the Fe-35Mn because balling decreases with remelting of the surface.[17] Since Fe-35Mn has a lower melting point (T_m at 1660 K) than pure Fe (T_m at 1810 K), [18,19] at higher energy densities the consolidated powder is remelted with subsequent passes. This can be seen from the surface morphology of Fe-35Mn at 133 J/mm^3 in Figure 2 (M-3), which is a characteristic of a remelted surface and also explains the decrease in S_a of Fe-35Mn at high energy densities. Furthermore, there exists a close correlation between the density and the roughness of the top surface. The mechanisms involved in the generation of higher surface roughness also introduce higher porosity. As depicted in Figure 1-B, the high surface roughness is correlated to the higher amount of internal defects as indicated by a lower density.

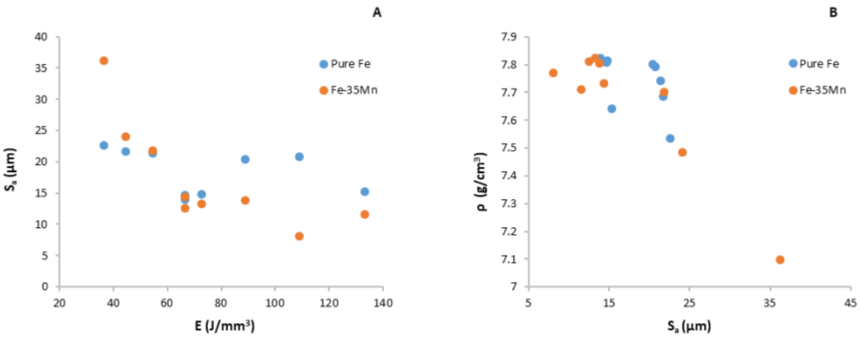

Fig. 1. (A) The effect of energy density on the surface roughness and (B) the effect of surface roughness on the density of bulk samples. Error bars are omitted due to the difficulty in resolving them beyond the markers.

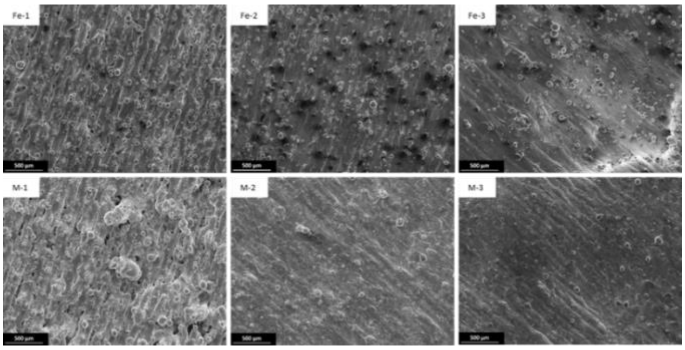

Fig. 2. Surface morphologies of as built bulk pure Fe and Fe-35Mn (M) with lowest energy density (1 at 36 J/mm^3), optimised energy density (2 at 67 J/mm^3) and highest energy density (3 at 133 J/mm^3). Build direction is out of plane.

3.2. *Density*

At lower energy densities the Fe-35Mn samples are significantly more porous than the pure Fe samples as can be seen from Figure 3. Both metals have small pores which are distinctive of partial melting, however, the Fe-35Mn has a significant number of larger pores. The larger solidification temperature range of the Fe-35Mn (≈ 50 K)[18] makes it more prone to shrinkage type defects than pure Fe with a narrow freezing range. As such, the pure Fe was generally easier to process for the bulk samples than the Fe-35Mn, which is further shown by the smaller variance in porosity with changing energy density.

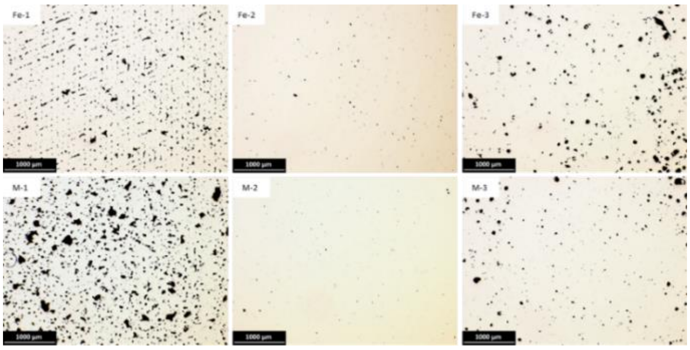

Fig. 3. Cross-sectional micrographs of as built bulk pure Fe and Fe-35Mn (M) with lowest energy density (1 at 36 J/mm^3), optimised energy density (2 at 67 J/mm^3) and highest energy density (3 at 133 J/mm^3). Build direction is out of plane.

For both pure Fe and the Fe-35Mn alloy, density and relative density increase with increasing energy density to a maximum between 60-80 J/mm$_3$, before decreasing as the energy density becomes too high as shown in Figure 4. The spherical pores observed in both metals at the highest energy density are formed due to gas entrapment during solidification in both alloys.[20] The pure Fe samples appears to have more of these pores, further shown by the lower relative densities at higher energy densities.

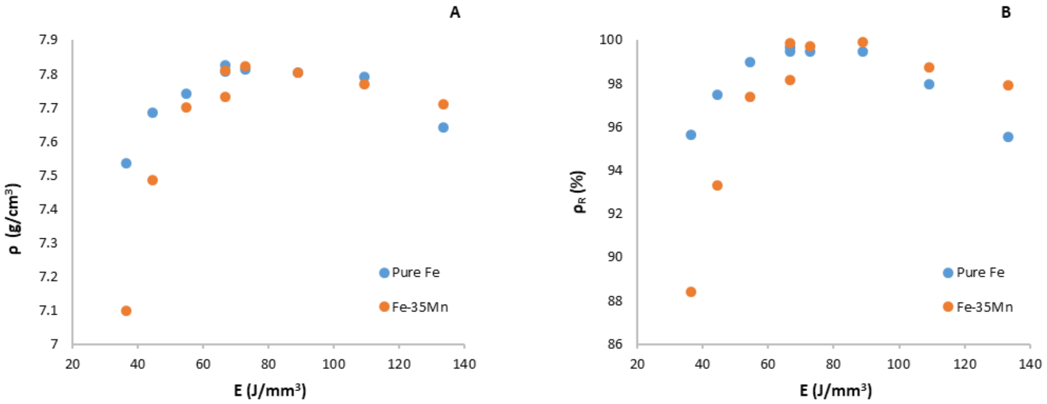

Fig. 4. The effect of energy density on the density (A) and relative density (B) of the bulk samples. Error bars are omitted due to the difficulty in resolving them beyond the markers

For bulk parts the main quality indicators are density and surface morphology. From Figure 3 and Figure 4 it can be seen that the parts with best surface morphology and highest density are those manufactured with an energy density of 67 J/mm$_3$ (Table 2).

Table 2 Processing parameters that produced best quality pure Fe and Fe-35Mn bulk component

Material	t_{on} (µs)	d_p (µm)	d_h (µm)	*Energy Density* (J/mm$_3$)
Pure Fe	100	60	100	67
Fe-35Mn	100	60	100	67

4. Conclusion

This study investigated the influence of SLM processing parameters on pure Fe and Fe-35Mn for biodegradable implant applications. Using a design of experiment approach the processing parameters were successfully optimised to achieve a relative density over 99.5 % for both pure Fe and Fe-35Mn. Overall, the pure Fe was easier to process than the Fe-35Mn because the lower melting temperature of the latter introduced large pores. In terms of process optimisation most of the quality indicators (surface roughness, density and relative density) could be correlated to the energy density.

Acknowledgments

DC, MJB and MSD acknowledge the support of the School of Mechanical and Mining Engineering, the Queensland Centre for Advanced Materials processing and Manufacturing and the Australian Research Council Research Hub for Advanced Manufacturing of Medical Devices (IH150100024). AGD, LC and BP acknowledge the support of European Union, Repubblica Italiana, Regione Lombardia and FESR for the project MADE4LO under the call "POR FESR 2014-2020 ASSE I -

AZIONE I.1.B.1.3". MJB also acknowledges the support of the Australian Research Council Discovery Program and is in receipt of Discover Early Career Researcher Award (DE160100260).

References

1. Zheng YF, Gu XN, Witte F. Biodegradable metals. Materials Science and Engineering: R: Reports. 2014;77:1-34.
2. Li H, Zheng Y, Qin L. Progress of biodegradable metals. Progress in Natural Science: Materials International. 2014;24(5):414-22.
3. Witte F. Reprint of: The history of biodegradable magnesium implants: A review. Acta Biomaterialia. 2015;23:S28-S40.
4. Bowen PK, Drelich J, Goldman J. Zinc Exhibits Ideal Physiological Corrosion Behavior for Bioabsorbable Stents. Advanced Materials. 2013;25(18):2577-82.
5. Mostaed E, Sikora-Jasinska M, Mostaed A, Loffredo S, Demir AG, Previtali B, et al. Novel Zn-based alloys for biodegradable stent applications: Design, development and in vitro degradation. Journal of the Mechanical Behavior of Biomedical Materials. 2016;60:581-602.
6. Peuster M, Wohlsein P, Brügmann M, Ehlerding M, Seidler K, Fink C, et al. A novel approach to temporary stenting: degradable cardiovascular stents produced from corrodible metal—results 6–18 months after implantation into New Zealand white rabbits. Heart. 2001;86(5):563.
7. Schinhammer M, Hänzi AC, Löffler JF, Uggowitzer PJ. Design strategy for biodegradable Fe-based alloys for medical applications. Acta Biomaterialia. 2010;6(5):1705-13.
8. Hermawan H, Dubé D, Mantovani D. Degradable metallic biomaterials: Design and development of Fe–Mn alloys for stents. Journal of Biomedical Materials Research Part A. 2010;93A(1):1-11.
9. Dargusch MS, Dehghan-Manshadi A, Shahbazi M, Venezuela J, Tran X, Song J, et al. Exploring the Role of Manganese on the Microstructure, Mechanical Properties, Biodegradability, and Biocompatibility of Porous Iron-Based Scaffolds. ACS Biomaterials Science & Engineering. 2019.
10. Fayazfar H, Salarian M, Rogalsky A, Sarker D, Russo P, Paserin V, et al. A critical review of powder-based additive manufacturing of ferrous alloys: Process parameters, microstructure and mechanical properties. Materials & Design. 2018;144:98-128.
11. Montani M, Demir AG, Mostaed E, Vedani M, Previtali B. Processability of pure Zn and pure Fe by SLM for biodegradable metallic implant manufacturing. Rapid Prototyping Journal. 2017;23(3):514-23.
12. Song B, Dong S, Deng S, Liao H, Coddet C. Microstructure and tensile properties of iron parts fabricated by selective laser melting. Optics & Laser Technology. 2014;56:451-60.
13. Li Y, Jahr H, Lietaert K, Pavanram P, Yilmaz A, Fockaert LI, et al. Additively manufactured biodegradable porous iron. Acta Biomaterialia. 2018;77:380-93.
14. Carluccio D, Demir AG, Caprio L, Previtali B, Bermingham M, Dargusch M. The Influence of Processing Parameters on Pure Fe and Fe-35Mn Scaffolds Produced by Selective Laser Melting. Journal of Manufacturing Processes, 40 (2019) 113-121.
15. ASTM International. Standard Test Methods for Determining Average Grain Size. PA, United States: ASTM International,; 2014.
16. Simchi A, Pohl H. Effects of laser sintering processing parameters on the microstructure and densification of iron powder. Materials Science and Engineering: A. 2003;359(1):119-28.
17. Li R, Liu J, Shi Y, Wang L, Jiang W. Balling behavior of stainless steel and nickel powder during selective laser melting process. The International Journal of Advanced Manufacturing Technology. 2012;59(9):1025-35.
18. Witusiewicz VT, Sommer F, Mittemeijer EJ. Reevaluation of the Fe-Mn phase diagram. Journal of Phase Equilibria and Diffusion. 2004;25(4):346-54.
19. Neubronner M, Bodmer T, Hübner C, Kempa PB, Tsotsas E, Eschner A, et al. D6 Properties of Solids and Solid Materials: Datasheet from VDI-Buch · Volume : "VDI Heat Atlas" in SpringerMaterials (https://dx.doi.org/10.1007/978-3-540-77877-6_26). Springer-Verlag.
20. Aboulkhair NT, Everitt NM, Ashcroft I, Tuck C. Reducing porosity in AlSi10Mg parts processed by selective laser melting. Additive Manufacturing. 2014;1-4:77-86.